

Jonathan M. Mihaly¹

Graduate Aerospace Laboratory,
California Institute of Technology,
Pasadena, CA 91125
e-mail: jmmihaly@caltech.edu

Jonathan D. Tandy

University of Leicester,
Leicester, UK
e-mail: jt245@leicester.ac.uk

A. J. Rosakis

Graduate Aerospace Laboratory,
California Institute of Technology,
Pasadena, CA 91125

M. A. Adams

Graduate Aerospace Laboratory,
California Institute of Technology,
Pasadena, CA 91125

D. Pullin

Graduate Aerospace Laboratory,
California Institute of Technology,
Pasadena, CA 91125

Pressure-Dependent, Infrared-Emitting Phenomenon in Hypervelocity Impact

A series of hypervelocity impact experiments were conducted with variable target chamber atmospheric pressure ranging from 0.9 to 21.5 Torr. Using a two-stage light-gas gun, 5.7 mg nylon 6/6 right-cylinders were accelerated to speeds ranging between 6.0 and 6.3 km/s to impact 1.5 mm thick 6061-T6 aluminum plates. Full-field images of near-IR emission (0.9 to 1.7 μm) were measured using a high-speed spectrograph system with image exposure times of 1 μs . The radial expansion of an IR-emitting impact-generated phenomenon was observed to be dependent upon the ambient target chamber atmospheric pressures. Higher chamber pressures demonstrated lower radial expansions of the subsequently measured IR-emitting region uprange of the target. Dimensional analysis, originally presented by Taylor to describe the expansion of a hemispherical blast wave, is applied to describe the observed pressure-dependence of the IR-emitting cloud expansion. Experimental results are used to empirically determine two dimensionless constants for the analysis. The maximum radial expansion of the observed IR-emitting cloud is described by the Taylor blast-wave theory, with experimental results demonstrating the characteristic nonlinear dependence on atmospheric pressure. Furthermore, the edges of the measured IR-emitting clouds are observed to expand at extreme speeds ranging from approximately 13 to 39 km/s. In each experiment, impact ejecta and debris are simultaneously observed in the visible range using an ultrahigh-speed laser shadowgraph system. For the considered experiments, ejecta and debris speeds are measured between 0.6 and 5.1 km/s. Such a disparity in observed phenomena velocities suggests the IR-emitting cloud is a distinctly different phenomenon to both the uprange ejecta and downrange debris generated during a hypervelocity impact. [DOI: 10.1115/1.4028856]

1 Introduction

In hypervelocity impact experiments, the ambient pressure P_{atm} in the target chamber has been shown to affect the observed impact phenomena, with both shock waves [1] and blast waves [2] having previously been reported. In this work, near-IR emission has also been observed to be affected by the ambient target chamber pressure. Preliminary results demonstrate a strong correlation between the size of a measured IR emitting region produced in experiments and the atmospheric pressure conditions within the target chamber. For example, a series of four IR images observed during impact experiments with ambient pressures ranging from 1.1 Torr to 21.5 Torr are presented in Fig. 1. The IR images display the total integrated emission seen by the detector over the length of the programed exposure time (1 μs). The position of the target, the direction of the incident impact vector, and artificial coloring has been added to the images presented in Fig. 1 to improve clarity. As observed, higher chamber pressures resulted in lower radial expansions of the subsequently measured IR-emitting cloud.

To investigate the observed pressure-dependence of the IR-emitting region, or cloud, a series of impact experiments were conducted with variable atmospheric target chamber pressures ranging from 0.9 to 21.5 Torr (146.7–2866.4 Pa). Dimensional analysis, originally presented by Taylor [3] on the expansion of a blast wave, is applied to describe the observed pressure-dependence of the IR cloud expansion. The atmospheric pressures considered are similar to those used in light-gas gun experiments

to enable drag-induced separation of sabots from impactors [4]. Therefore, observations of phenomena presented herein may have broad implications on hypervelocity impact testing. Furthermore, the range of atmospheric pressure conditions considered are similar to those considered in previous work by Schultz and Sugita on impact-induced emission [5–9].

2 Experimental Setup

The two-stage light-gas gun in the SPHIR facility [1] located at the California Institute of Technology was used to conduct a series of experiments with variable target chamber atmospheric pressures ranging from 0.9 to 21.5 Torr. This facility has previously been used in a number of previous works [10,11] to accelerate small particles to hypervelocities for experimental comparisons with numerical models. In this work, Nylon 6/6 right cylinders ($d = 1.8 \text{ mm}$, $l/d = 1$) were accelerated to impact speeds ranging from 6.0 to 6.6 km/s. Cylindrical projectiles were used given the inability to consistently launch spherical projectiles at the time of this work. The series of five experiments considered herein use $h = 1.5 \text{ mm}$ thick aluminum 6061-T6 target plates with dimensions $150 \text{ mm} \times 150 \text{ mm}$. Impact obliquity was held constant at 0 deg (normal impact). Table 1 provides a summary of the experimental parameters of the five considered experiments. Only experimental results with IR images produced using an exposure time of 1 μs are considered. The effective time of each image (presented in Table 1 as t_{IR}) is the sum of the exposure time (1 μs) and delay time (after impact) of each image.

Multiple diagnostics were utilized during each experiment. A Princeton Instruments spectrometer system was used to capture a single full-field image of near-IR (0.9 μm to 1.7 μm) emission from both uprange and downrange phenomena. This system utilized an Acton SP2560 spectrograph coupled with a high-speed

¹Corresponding author.

Contributed by the Applied Mechanics of ASME for publication in the JOURNAL OF APPLIED MECHANICS. Manuscript received June 2, 2014; final manuscript received October 17, 2014; accepted manuscript posted October 21, 2014; published online November 19, 2014. Editor: Yonggang Huang.

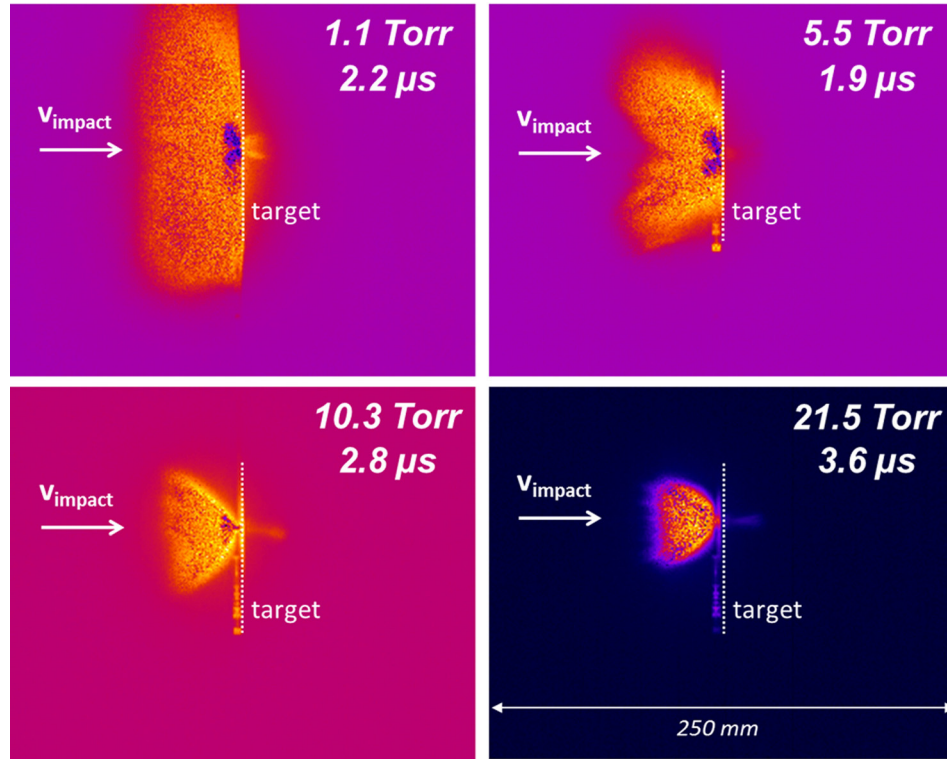


Fig. 1 IR images for four experiments with a range of ambient chamber pressures. Times in microseconds indicate time after impact. Images shown with false color to add contrast.

OMA-V camera (minimum exposure time $1 \mu\text{s}$), with a 320×256 pixel liquid nitrogen cooled InGaAs detector array. The OMA camera is operated by the WINSPEC32 software provided by Princeton Instruments. This near-IR spectrograph system is mounted above the SPHIR target chamber and oriented at an angle of approximately 27° from vertical with a field-of-view of $25.1 \text{ cm} \times 20.0 \text{ cm}$ [1]. The exposure time for each IR image was (the minimum available) $1 \mu\text{s}$.

Full-field IR emission images were complemented by laser side-lighting (LSL) shadowgraphs [12]. The LSL system uses collimated, coherent illumination to provide a series of shadowgraph images describing the formation and propagation of ejecta and debris phenomena in each experiment. Images are taken with an ultrahigh-speed Cordin 214-8 camera which provides exposure and interframe times as low as 10 ns . Such exposure time enables sharp visualization of impact features with very little motion blur at the observed impact speeds around 6 km/s .

3 Dimensional Analysis of a Point-Blast Explosion

Dimensional analysis described originally by Taylor [3] (see also Whitham [13], p. 192) can be used to describe the pressure-dependent expansion of a blast wave produced in an explosion. The explosion is idealized as a sudden, symmetrical release of energy E concentrated at a point. It is also assumed that energy is

the only dimensional parameter introduced by the explosion. Last, the disturbance is assumed sufficiently strong such that the initial pressure and sound speed of the ambient air are negligible compared to the pressures and velocities in disturbed flow. In this case, strong shock relations apply. With these assumptions, the only dimensional parameter relating to the ambient gas is density ρ [13].

The only parameter involving length and time is given by E/ρ_0 , with dimensions L^5/T^2 . It then follows that the functional dependence of the shock radius at time t , namely $R = R(E, \rho_0, t)$, must be of the form given by Eq. (1), where K is a dimensionless number. It is now assumed that the energy E that generates the blast wave can now be expressed as a fraction of the incident kinetic energy of the impactor by Eq. (2), where m is the mass of the impactor, v its speed, and α the fraction of the incident impactor kinetic energy going into the blast wave. At the lowest chamber pressure considered (0.9 Torr), the particle mean free path is approximately $50 \mu\text{m}$ [14] and, therefore, continuum theory is applicable. Assuming the fluid in the target chamber is an ideal gas, the density of the ambient air can be computed given the target chamber's atmospheric pressure (in Torr) as described in Eq. (3)

$$R(t) = K \left(\frac{E}{\rho_0} \right)^{1/5} t^{2/5} \quad (1)$$

$$E = \frac{1}{2} \alpha m v^2 \quad (2)$$

$$\rho_0 = \frac{P_{\text{atm}}}{R_{\text{gas}} T} \quad (3)$$

Along with the definition of available energy Eq. (2), the ideal gas equation can then be substituted into the dimensional analysis solution for blast wave radius Eq. (1). The predicted radius Eq. (4) can then be determined as a function of the experimental parameters and a dimensionless constant C Eq. (5), which includes the dimensionless parameters K and α

Table 1 Parameters of the experiments considered for dimensional analysis

ID	P_{atm} (Torr)	v (km/s)	m (mg)	t_{IR} (μs)
A1	0.9	6.00	5.77	2.3
A2	1.1	6.18	5.72	2.2
A3	5.5	6.32	5.63	1.9
A4	10.3	6.25	5.73	2.8
A5	21.5	6.05	5.67	3.6

$$R(t) = C \left(\frac{mv_{\text{impact}}}{P_{\text{atm}}} \right)^{1/5} t^{2/5} \quad (4)$$

$$C = 3.16K\alpha^{1/5} \quad (5)$$

4 Analysis

The analysis presented herein investigates whether the observed pressure dependence of the IR-emitting region can be described by the dimensional analysis for blast waves by Taylor. This requires a comparison of the experimentally measured radii of the IR-emitting region (R_{exp}) with the radii predicted by the Taylor blast wave theory R_T . Such a comparison requires the measurement of the empirically observed radii and the determination of parameters K and α from Eqs. (1) and (2).

4.1 Definition of IR-Emitting Cloud Radius. Measurement of the experimentally observed IR-emitting cloud radius R_{exp} is challenging, as they are often highly asymmetric. Such asymmetry is not surprising, considering that the mass of ejecta following the impact is not symmetric, as observed in the LSL results. Furthermore, as a consequence of the relatively slow exposure time ($1 \mu\text{s}$) with respect to the blast wave speed, the boundary of the observable IR-emitting areas is a gradual transition in grayscale.

Therefore, analysis of the presented IR images requires a consistent method to define the radius of the IR-emitting cloud. To define a threshold value to differentiate between the IR-emitting cloud and the background, the empirical CDF (cumulative distribution function) of the grayscales of the image pixels (uprange from the target) is considered by ranking pixel grayscales. The threshold levels for each image are then defined as the grayscales corresponding to cumulative probabilities of $p = 95\%$ on the CDF. An example of CDF, describing the IR image taken with $P_{\text{atm}} = 5.5 \text{ Torr}$, is provided in Fig. 2.

To isolate the IR-emitting region, image thresholding is performed on each IR image using the $p = 95\%$ threshold grayscale definition. The remaining pixels in the resulting image are then considered in a radial coordinate system, where the impact position is the origin and $\theta = 0$ corresponds to upward direction along the vertical axis in the IR image. The boundary of the IR-emitting region is then determined for each angle θ from 0 to 180, with steps of one degree, by taking the average of the three largest corresponding radial coordinates. The observed radius of the IR-emitting region (R_{exp}) for each IR image is then defined as the maximum observed boundary radius for any θ . This definition therefore facilitates the theoretical prediction of the farthest expansion of IR-emitting cloud. An example of this process for the $p = 5.5 \text{ Torr}$ experiment is provided in Fig. 3.

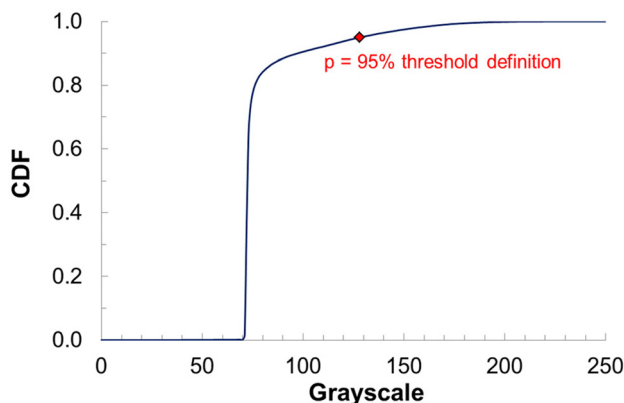


Fig. 2 CDF of an IR image pixel grayscale distribution and the $p = 95\%$ grayscale used to define the image threshold value

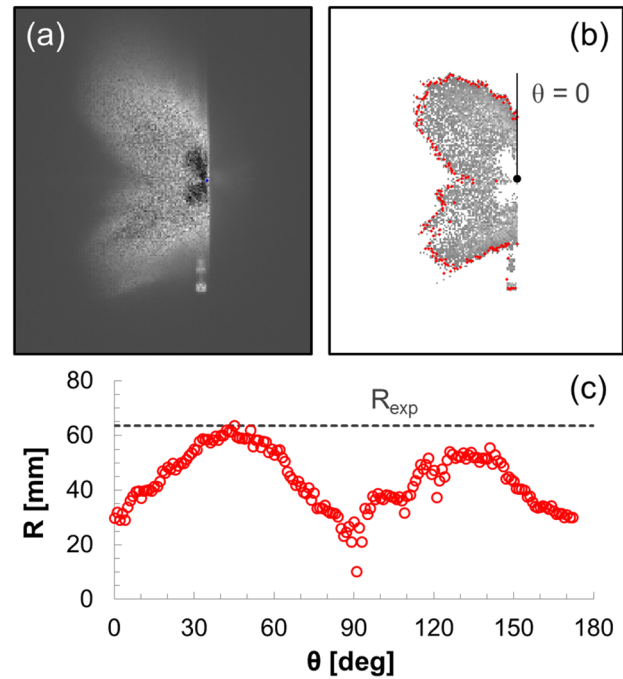


Fig. 3 (a) Cropped IR image before grayscale level thresholding, (b) IR image after grayscale thresholding based on the $p = 95\%$ grayscale level, and (c) R-theta plot of the boundary pixels in the IR image and definition of the experimentally observed radius, R_{exp}

The results for implementing this radius-defining process on each of the five primary experiments considered are presented in Fig. 4. As shown, the $p = 95\%$ threshold level definition and subsequent process produces observed radii that adequately describe the farthest propagation of the IR-emitting cloud. The consideration of other threshold definitions, such as $p = 90\%$ and $p = 99\%$, facilitates the estimation of the uncertainty in the experimentally observed IR cloud radii.

4.2 Determination of Blast-Wave Dimensional Analysis Constants. The parameters K and α are first considered as empirically fit parameters. Given that α is defined as the percent of the impactor's incident kinetic energy used in forming the blast wave, α must be less than 1. The optimum K and α are then determined by minimizing the root-mean-square (RMS) error between R_{exp} and R_T using a least-squared minimization routine. Considered values for α ranged from 0 to 1 with increments of 0.01. Preliminary correlation analysis indicated that values for $K < 4$ would best describe the data. Considered values for K were then considered from 0 to 4 with increments of 0.01.

Whitham describes Taylor's constant K in Eq. (1) as a dimensionless number that is fixed from the definition of E as the total energy in the flow [13]. An analytical solution for constant K is provided by Taylor, who describes K as a function of only the ratio of specific heats γ [3]. This is an idealized assumption for a spherical blast wave. The radius of the blast wave, R , is thus described by Taylor by Eq. (6)

$$R = K(\gamma) \left(\frac{E}{\rho_0} \right)^{1/5} t^{2/5} \quad (6)$$

The constant K is fixed from the definition of the total energy in the flow [13]. Taylor defines the energy in the flow using contributions from both kinetic energy and heat energy. Using similarity assumptions and dimensional analysis, Taylor provides an approach to numerically determine the effective K for a given

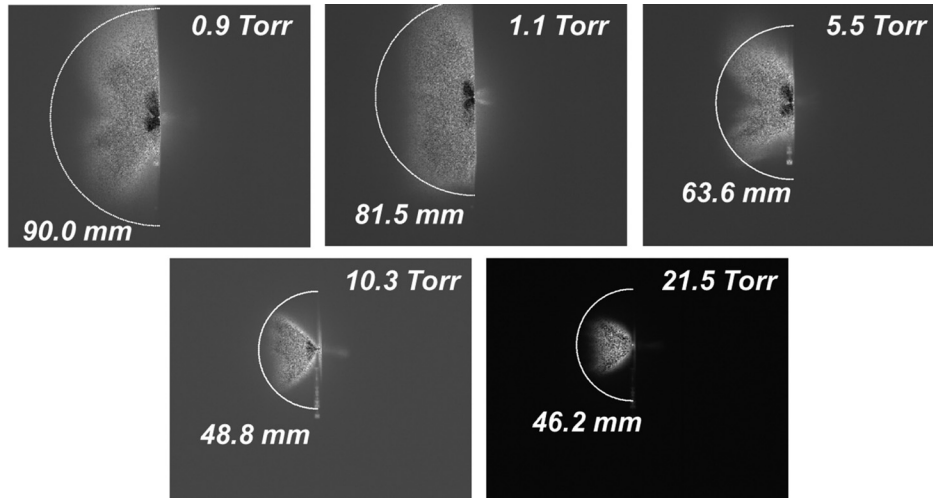


Fig. 4 Radii of IR cloud expansion measured for each IR image considered

value of γ [3]. For $\gamma = 1.4$, corresponding to air, K is approximated as 1.03. For $\gamma = 5/3$, the value of K is found to be 1.13.

4.3 Uncertainty in Experimental and Theoretical Results.

A full comparison of results requires consideration of the uncertainty in both the empirically measured cloud radii and theoretically predicted blast wave radii. The uncertainty of the experimental results is characterized by the range of maximum cloud radii measured by varying the threshold definition on each image's grayscale CDF (described in Sec. 4.1) from 90% to 99%.

The uncertainty in the predicted blast wave radius from the Taylor theory is characterized accounting for experimental uncertainties in the measurement of impactor mass, velocity, chamber pressure, and image time. The root-sum-square (RSS) error of the product of the partial derivatives of Eq. (4) and corresponding parameter uncertainties is used to estimate the uncertainty in the dimensional analysis predicted radius in Eq. (7). The uncertainties for the effective time for each image are described in Table 2. The uncertainty in the measurement of impactor velocities for each experiment was 0.1 km/s. A detailed description of the determination of effective image time and impact velocity is provided in previous work [1]. Chamber pressure and impactor mass have uncertainties of 0.2 Torr and 0.1 mg, respectively, based upon the consistency of repeated measurements before and during the conducted experiments

$$\varepsilon_R = \sqrt{\left(\frac{\partial R}{\partial m} \varepsilon_m\right)^2 + \left(\frac{\partial R}{\partial v} \varepsilon_v\right)^2 + \left(\frac{\partial R}{\partial P_{\text{atm}}} \varepsilon_{P_{\text{atm}}}\right)^2 + \left(\frac{\partial R}{\partial t} \varepsilon_t\right)^2} \quad (7)$$

Table 3 provides a comparison between the total uncertainty ($\varepsilon_{R+} + \varepsilon_{R-}$) in the experimentally measured IR expansion radii R_{exp} and the distance D traversed by the front predicted by the Taylor analysis. The instantaneous velocity of the shock front can be obtained by differentiating Eq. (4). By integrating the shock velocity over the exposure time of the IR image, the distance

Table 2 Uncertainties for the effective time of the IR images in microseconds

ID	t_{IR}	ε_t
A1	2.3	0.14
A2	2.2	0.14
A3	1.9	0.10
A4	2.8	0.16
A5	3.6	0.19

Table 3 Comparison between total uncertainty in the experimentally measured IR expansion radii R_{exp} and the predicted distance D traversed by the front predicted by the Taylor analysis. All units presented in mm.

ID	$\varepsilon_{R+} + \varepsilon_{R-}$	D
A1	24.0	17.3
A2	19.2	17.4
A3	23.9	14.5
A4	22.6	9.3
A5	21.0	6.5

traversed by the front is estimated for each experiment to range from 6 to 17 mm. The total uncertainties in the measured IR expansion radii therefore cover a conservative range, greater than that traversed by the front during the image exposure time. As such, the determined uncertainties ε_{R+} and ε_{R-} are sufficient to account for the high-speed expansion and relatively long exposure time of the IR image.

5 Results

Using the experimentally measured radii presented in Fig. 4, the optimum dimensionless parameters K and α were determined using the previously described least-squares RMS error routine. This routine is applied to determine the empirically observed K and α by first considering all of the experiments. Because the Taylor blast wave analysis was derived considering ambient levels of atmospheric pressure, the optimum values for K and α were also determined for the two experiments with the highest atmospheric pressures (10.3 Torr and 21.5 Torr). Figure 5 plots K corresponding to the lowest RMS error as a function of α , for results fitting all five considered experiments and also fitting just the two highest pressure experiments. As shown in Fig. 6, the corresponding minimum RMS error as a function of α is approximately constant (to within 3×10^{-3}). Therefore, the curves presented in Fig. 5 represent the locus of combinations for K and α which yield the same predictions for blast wave radii. Note the results shown in Fig. 6 correspond to the case considering all experiments, but this result has been observed for all parameter-fitting results for K and α .

Using the solution family for K and α considering all five experiments, the resulting predictions for blast wave radii R_T are compared to the experimentally observed radii R_{exp} . A direct comparison of the experimental and theoretical results is presented in Fig. 7 and Table 4. Overall, the dimensional analysis solutions for the blast-wave radii describe the observed radii largely within the described uncertainties. In Fig. 8, the theoretically predicted blast

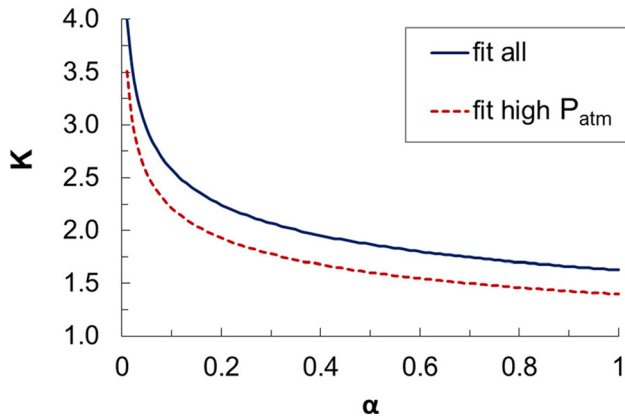


Fig. 5 Optimum value of K (lowest RMS error) versus α determined empirically by considering all five experiments for $h = 1.5$ mm target plates. The results for K versus α determined using only the two higher chamber pressure experiments are also presented.

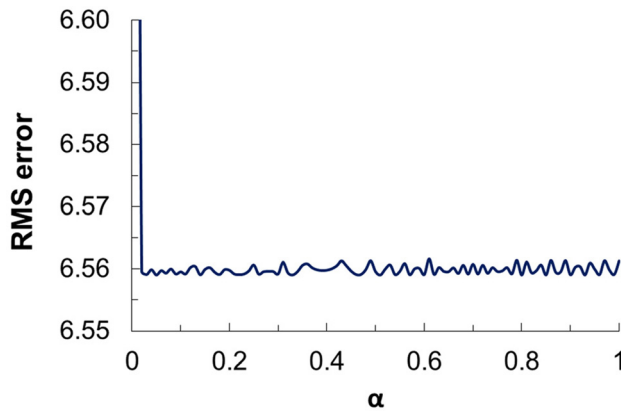


Fig. 6 Minimum RMS error as a function of α

waves are overlaid on the corresponding IR images for each experiment. Graphically, the predicted blast waves provide an estimation of the expansion of the observed IR-emitting phenomena.

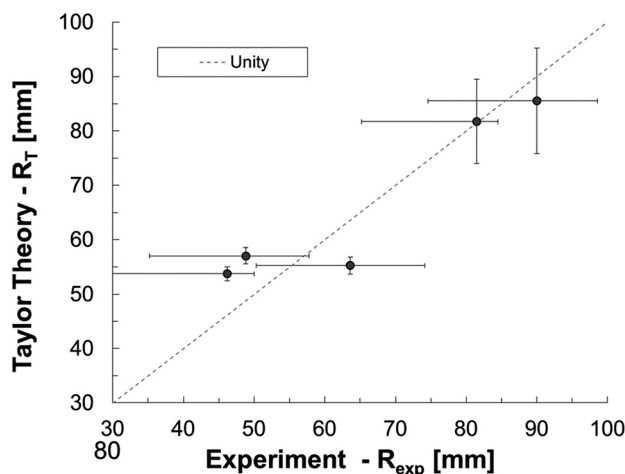


Fig. 7 Measured expansion radii versus the predicted radii using the Taylor dimensional analysis and empirically determined values for K and α

Table 4 Summary of results for experimentally measured IR expansion radii R_{exp} , predicted Taylor blast wave radii R_T , and corresponding values of uncertainty. All units presented in mm.

ID	R_{exp}	ε_{R+}	ε_{R-}	R_T	ε_{R_T}
A1	90.0	8.6	15.4	85.5	9.7
A2	81.5	3.0	16.3	81.7	7.7
A3	63.6	10.6	13.3	55.3	1.6
A4	48.8	9.0	13.6	57.1	1.5
A5	46.2	3.8	17.2	53.7	1.3

Figure 9 provides another graphical comparison of the observed radii with the theoretically predicted results using the empirically determined values for K and α . In this figure, the experimental results are plotted against the radii predicted by dimensional analysis as a function of target chamber pressure. Each experiment produces a different radius-curve as a function of chamber pressure, given small differences in the parameters presented in Table 1. The uncertainty in each curve, described by Eq. (7), is included and incorporates the contribution of the experimental uncertainty in chamber pressure. The uncertainty of the experimentally measured radii, determined as described in Sec. 4.1, is also included. Plotted in terms of chamber pressure, the experimentally observed radii conform to the characteristic nonlinear decay as a function of pressure.

6 Discussion

As presented, the dimensional analysis solution by Taylor [3,13] for the radial position of a blast wave describes the observed pressure-dependent expansion of an IR-emitting cloud following impact. The optimum value for the dimensionless parameter K is observed to be $K > 1.63$ when determined from results for all five experiments. However, as described by Taylor [3], the expected value for K in air ($\gamma = 1.4$) is $K = 1.03$. For $\gamma = 5/3$, $K = 1.13$. Note that the theoretical predictions for K include no assumption about the value for α . The maximum radii (corresponding to $\alpha = 1$) for the idealized values of K ($\gamma = 1.4$ and $\gamma = 5/3$) are presented in Table 5 along with the predicted values from the empirically determined K . The notional use of $\alpha = 1$ in Table 5 provides the limiting case and minimum disparity between purely theoretical and observed experimental results. Therefore, as presented in Table 5, the ideal theoretical values for K underpredict both the results using the empirically determined K and the observed IR-emitting cloud radii.

It is unlikely that this disparity is the result of a systematic error in the determination of the effective time-after-impact, t_{IR} , of each image. The effective image time t_{IR} is affected by the delay between impact (first contact of impactor and target) and the triggering of the high-speed diagnostics. This delay is estimated through measurement of the ejecta speed thrown uprange in each experiment [1] and does not include the inertial delay between impact and the release of visible ejecta. To account for the discrepancy described in Table 5, an additional time-delay between 2 and $4 \mu s$ would have to be added to each IR image's effective time. Such a delay is infeasible given that this time would correspond to multiple transits of the shock wave within the target plate and is inconsistent with observations from the LSL system of ejecta speed and position [1].

Taylor's dimensional analysis assumes idealized, symmetrical conditions for a spherical blast-wave. The impact experiments feature tumbling cylinders and asymmetric impact conditions, as observed in the LSL system. Therefore, the discrepancy between ideal theoretical and empirically optimum K values could be a consequence of the nonsimplified impact conditions in the experiments.

Additionally, what is not accounted for in the consideration of the incident impactor energy is the kinetic energy associated with

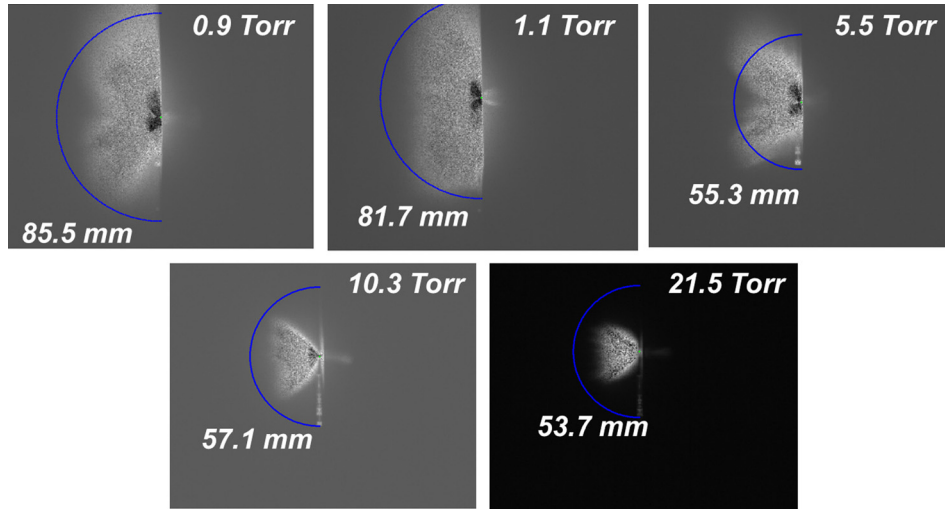


Fig. 8 Predicted radii of the IR cloud expansion for each IR image using the Taylor blast wave dimensional analysis and empirically determined values for K and α

the tumbling of the impactor. Cylindrical impactors have been observed to tumble, at times, with angular velocities of at least 250,000 rpm [1]. At 6.2 km/s, this corresponds to rotational energy that is approximately 7% of the incident impactor kinetic energy. Such an increase in available kinetic energy is capable of changing the predicted radii by a few millimeters and improving the agreement between experimentally measured and predicted radii.

7 Discussion on the Rapidly Expanding IR Phenomena

Given the measured radius of expansion at the time of each presented image, the defined fronts of the IR-emitting clouds have observed velocities ranging from 12.8 km/s (for the 21.5 Torr, 1.5 mm plate) to 39.1 km/s (for the 0.9 Torr, 1.5 mm plate experiment). The instantaneous blast wave velocities described by the Taylor dimensional analysis ranges from 6.0 km/s (for 21 Torr at 3.6 μ s) to 14.7 km/s (for 0.9 Torr at 2.3 μ s after impact). In comparison, the ejecta and debris phenomena observed with the LSL system produce substantially slower velocities ranging between 0.6 and 5.1 km/s [1]. Such a disparity suggests that the IR-emitting cloud is a distinctly different phenomenon to both the uprange ejecta and downrange debris observed using the LSL technique.

Consider an example of a hypervelocity impact experiment on a double-plate system with concurrent measurement of impact

phenomena. Two $h=0.5$ mm plates are mounted in the SPHIR target chamber with 50 mm of separation. The spacing and thicknesses of the target configuration are characteristically similar to those used in spacecraft shielding systems [2]. The target configuration is then impacted by a 5.59 mg nylon 6/6 equiaxed cylinder at 6.53 km/s. Figure 10 provides the sequence of shadowgraph images produced by the LSL system. Analysis of the formation of uprange ejecta provides an estimate for trigger delay time of 2.9 μ s [1] (therefore, the images presented in Fig. 11 are labeled with respect to the time after impact).

As presented in Fig. 10, the debris cloud is observed to travel downrange with a shot-line velocity of 5.1 km/s. By the fifth frame at 13.2 μ s after impact, the debris cloud has impacted the second plate and by 23.2 μ s, the rear-wall plate has been perforated. A visible emitting phenomenon is then observed to travel back uprange and interact with the downrange face of the first target.

The complementary measurement of IR emission for this experiment, at 4.2 μ s after impact, is presented in Fig. 11. The figure presents the IR image and the corresponding LSL image taken at the same time. The field of view of the LSL system is depicted on the IR image. At 4.2 μ s after impact, the IR-emitting cloud is observed to be interacting with the second plate 50 mm downrange, while the observable debris in the LSL image has only propagated 12.8 mm downrange.

Given the LSL results and measured debris cloud speed, backward extrapolation from the observed debris cloud position estimates that the IR image corresponds to 3.4 μ s after the debris was thrown from the back-surface of the target plate. Given this time and a 50 mm separation distance between the two-plates, the minimum speed of the IR-emitting cloud observed downrange striking the rear-wall plate is approximately 14.5 km/s.

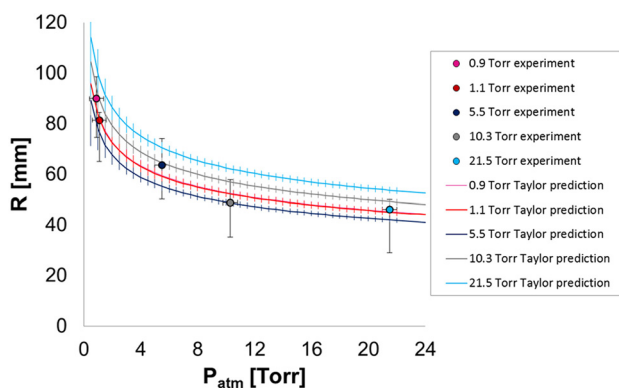


Fig. 9 Measured expansion radii versus the corresponding predicted radius as a function of pressure for each impact experiment

Table 5 Comparison of the experimentally observed expansion radii, the theoretically predicted radii for the idealized values of K , and the lowest empirically determined value for K . All radii presented in mm.

ID	R_{exp}	$R_T (K = 1.03)$	$R_T (K = 1.13)$	$R_T (K = 1.63)$
A1	90.0	54.0	59.3	85.5
A2	81.5	51.6	56.6	81.7
A3	63.6	34.9	38.3	55.3
A4	48.8	36.1	39.6	57.1
A5	46.2	34.0	37.3	53.7

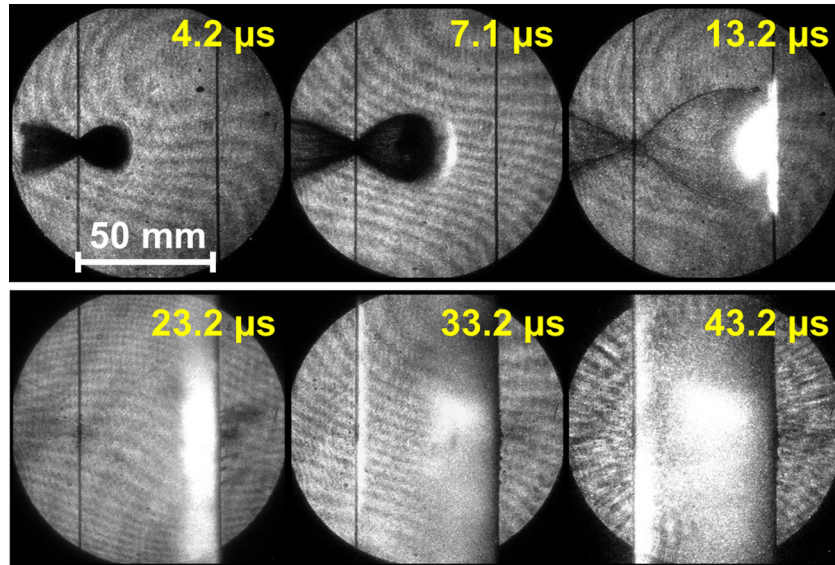


Fig. 10 LSL system results for a double-plate target configuration. Two $h = 0.5$ mm target plates, with 50 mm separation, are impacted by a 5.59 mg nylon cylinder at 6.53 km/s. Timestamps shown indicate image time after impact.

In the LSL image shown in Fig. 11, there is no observable aberration in grayscale beyond the observed debris cloud. The LSL image was taken at the lowest possible illumination source intensity, 60 mW. Given the 100 mm diameter illuminated field of view, the background illumination density in the LSL image presented in Fig. 11 is 7.64 W/m^2 . With this configuration, the system is most sensitive to variations in optical density of the fluid medium surrounding the target. Therefore, given this evidence, it is likely the source of IR emission interacting with the downrange second target plate is of negligible mass. Furthermore, given the observable spectrum of the Cordin camera from 400 nm to 900 nm, there is no complementary emission in the visible range with greater than 7.64 W/m^2 intensity.

The images presented in Fig. 11 demonstrate the different phenomena observed using the IR and LSL imaging systems. Primarily, the scale of the uprange IR-emitting cloud is significantly

larger than the ejecta material concurrently observed in the LSL system [1]. However, the shape of the phenomena observed in the LSL and IR images is strikingly similar. In particular, direct comparison of the IR and LSL images presented in Fig. 11 indicates that the darker region in the uprange and downrange IR-emitting cloud are of the same shape and scale as the debris material observed in the LSL image. This suggests the formation of the IR-emitting cloud is related to the debris observed with the LSL system. A thorough discussion of the size, shape, and temporal evolution of the observed IR-emitting phenomena is presented in a previous work [15].

The majority of the observed IR-emission is likely produced by a relatively diffuse vapor/plasma cloud [1,15], similar to that observed by Sugita and Schultz [7,9,16]. They describe an impact-induced vapor cloud as a chemically and thermally heterogeneous entity with components each having different mass,

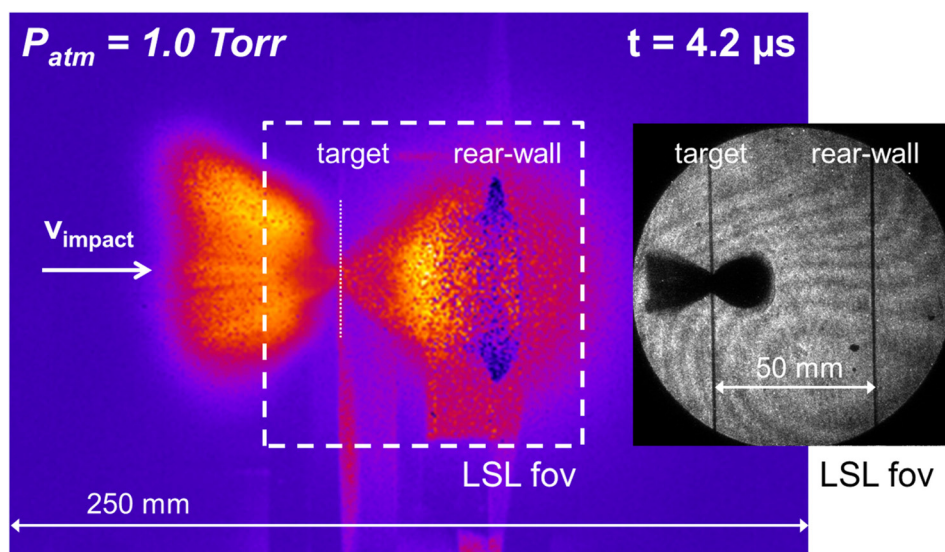


Fig. 11 Concurrent IR and LSL image results for a 6.53 km/s impact on a double-plate target configuration consisting of two 0.5 mm aluminum plates separated with a 50 mm stand-off distance

momentum, and energy [9]. Thermal modeling of the impact-induced vapor cloud by Sugita suggests that high-temperature radiation observed in hypervelocity impact experiments is attributed to ablation vapor from the surface of extremely small, high-speed fragments entrained in the vapor cloud [16]. Another potential hypothesis is that the front of the observed IR-emitting phenomenon consists of charged particles ejected at extreme speeds from the impact. The fast, charged particles would overtake a blast wave or vapor front as they travel downrange.

The damage induced by vapor clouds to impact shielding rear-walls is well-documented [2]. Rear-walls of bumper shields must be made massive enough to prevent spallation and buckling in response to the blast wave loading of the vapor clouds. However, for the observed IR-emitting phenomenon interacting with the rear-wall in Fig. 11, simultaneous results from the LSL system indicate no measurable mechanical response or deformation on the rear-wall. Results from similar experiments configured with thinner rear-walls of films and foils also indicate no measurable mechanical response of the rear-wall in conjunction with the arrival of the observed IR-emitting phenomenon with the rear-wall.

Previous and ongoing research investigating plasmas produced during hypervelocity impact suggest the generation of electrical phenomena is capable of damaging spacecraft systems [17]. It is also currently unknown if the IR-emitting phenomenon observed to interact with the rear-wall delivers a charge.

Analysis of concurrently measured UV-Vis spectra indicates strong emission in the regions of observed debris from species originating from the nylon impactor [1,15]. Such results may provide insight into the origin and composition of the observed IR-emitting phenomena. However, the characterization of the IR-emitting materials on the leading edges of the observed IR-emitting clouds would be challenging, given the high-speed of the observed front.

8 Conclusion

The radial expansion of the observed IR-emitting phenomenon is demonstrated to be dependent on the ambient atmospheric pressure in the target chamber. Dimensional analysis by Taylor [3] for the expansion of a spherical blast wave is shown to describe the nonlinear, pressure-dependent expansion of the experimentally measured IR-emitting regions. Refinement of the pressure-dependent observation and analysis presented herein has the potential to provide insight into the amount of impactor kinetic energy dissipated through the formation of a blast wave. The future availability of high-speed near-IR cameras capable of sub-microsecond exposure time would greatly support such refinement by significantly reducing the uncertainty in the measurement of the IR-emitting phenomenon's expansion. Additionally, the use of spherical projectiles in future investigations would enable further improvement by eliminating the potential error source attributed to projectile tumbling.

The atmospheric pressures considered herein are similar to those used in light-gas gun experiments to enable drag-induced separation of sabots from projectiles. Therefore, given current procedures typically used in hypervelocity impact testing, the observed pressure-dependent expansion of IR-emitting material has implications on the results in both previous and current hypervelocity impact investigations. Without the use of a high-speed IR camera, concurrently operated with a high-speed imaging system, the reported IR-emitting phenomenon would be unobserved and uncharacterized.

Furthermore, comparison of the IR and LSL images indicates two distinctly different, yet interrelated, phenomena. The high-speed, IR-emitting cloud is observed in experiments to expand at velocities much higher than the debris and ejecta phenomena observed using the LSL system. In a double-plate target configuration, representative of geometries used in spacecraft shielding, this IR-emitting phenomena is observed to reach the rear-wall

several μ s before the debris cloud. Although no mechanical effects are observed on the rear-wall in response to the IR-emitting cloud, the implications of this phenomenon on hypervelocity impact shield design are currently unknown. Future work is required to investigate the composition and potential charge of the IR-emitting phenomenon. However, the repeatable occurrence of an IR-emitting phenomenon interacting with a rear-wall, independent of the subsequent debris cloud, has been observed and characterized for the first time.

Acknowledgment

This material is based upon work supported by the Department of Energy National Nuclear Security Administration under Award No. DE-FC52-08NA28613. The authors would also like to thank Michael Mello for his assistance with the optomechanical design of the LSL system and Petros Arakelian for his assistance in installing the optical benches and safety feature.

Nomenclature

D	= distance traveled by Taylor blast-wave
E	= impact kinetic energy
h	= target thickness
K	= dimensionless number in blast-wave analysis
m	= impactor mass
P_{atm}	= ambient pressure
R	= blast wave radius
R_{exp}	= blast wave radius observed in experiment
R_{gas}	= ideal gas constant
R_{T}	= blast wave predicted by Taylor blast-theory
t	= time after impact
t_{IR}	= completion time of IR image
α	= fraction incident impactor KE partitioned to blast-wave
γ	= ratio of specific heats
ε	= uncertainty
v	= impact speed
ρ_0	= atmospheric density

References

- [1] Mihaly, J. M., Tandy, J. D., Adams, M. A., and Rosakis, A. J., 2013, "In Situ Diagnostics for a Small-Bore Hypervelocity Impact Facility," *Int. J. Impact Eng.*, **62**, pp. 13–26.
- [2] Christiansen, E., 2009, *Handbook for Designing MMOD Protection*, NASA, Washington, DC, Technical Memorandum No. TM-2009-214785.
- [3] Taylor, G. I., 1950, "The Formation of a Blast Wave by a Very Intense Explosion. I. Theoretical Discussion," *Proc. R. Soc. Lond. Ser. A*, **201**(1065), pp. 159–174.
- [4] Piekutowski, A. J., and Poorman, K. L., 2013, "Effects of Scale on the Performance of Whipple Shields for Impact Velocities Ranging From 7 to 10 km/s," *Procedia Engin.*, **58**, pp. 642–652.
- [5] Schultz, P. H., Adams, M. A., Perry, J. W., Goguen, J. D., and Sugita, S., 1996, "Impact Flash Spectroscopy," 27th Lunar and Planetary Science Conference (LPSC 96), Houston, TX, Mar. 18–22, Paper No. 1575.
- [6] Sugita, S., Schultz, P., and Adams, M., 1997, "In Situ Temperature Measurements of Impact-Induced Vapor Clouds With a Spectroscopic Method," 28th Lunar and Planetary Science Conference (LPSC 97), Houston, TX, Mar. 17–21, pp. 1149–1150, Paper No. 1306, available at: <http://www.lpi.usra.edu/meetings/lpsc97/pdf/1306.PDF>
- [7] Sugita, S., and Schultz, P., 1998, "Spectroscopic Observation of Atmospheric Interaction of Impact Vapor Clouds," 29th Lunar and Planetary Science Conference (LPSC 98), Houston, TX, Mar. 16–20, Paper No. 1751, available at: <http://www.lpi.usra.edu/meetings/LPSC98/pdf/1751.pdf>
- [8] Sugita, S., and Schultz, P., 2000, "Spectroscopic Observation of Chemical Interaction Between Impact-Induced Vapor Clouds and the Ambient Atmosphere," 31st Lunar and Planetary Science Conference (LPSC 2000), Houston, TX, Mar. 13–17, Paper No. 2029, available at: <http://www.lpi.usra.edu/meetings/lpsc2000/pdf/2029.pdf>
- [9] Sugita, S., and Schultz, P. H., 2003, "Interactions Between Impact-Induced Vapor Clouds and the Ambient Atmosphere: 1. Spectroscopic Observations Using Diatomic Molecular Emission," *J. Geophys. Res.*, **108**(E6), p. 5051.
- [10] Adams, M., Lashgari, A., Li, B., McKerns, M., Mihaly, J., Ortiz, M., Owahdi, H., Rosakis, A., Stalzer, M., and Sullivan, T., 2012, "Rigorous Model-Based Uncertainty Quantification With Application to Terminal Ballistics, Part II.

- Systems With Uncontrollable Inputs and Large Scatter," *J. Mech. Phys. Solids*, **60**(5), pp. 1002–1019.
- [11] Kanga, P. H. T., Li, B., McKerns, M., Nguyen, L. H., Ortiz, M., Owhadi, H., and Sullivan, T. J., 2014, "Optimal Uncertainty Quantification With Model Uncertainty and Legacy Data," *J. Mech. Phys. Solids*, **72**, pp. 1–19.
- [12] Mihaly, J. M., Rosakis, A. J., Adams, M., and Tandy, J., 2013, "Imaging Ejecta and Debris Cloud Behavior Using Laser Side-Lighting," *Procedia Engineering*, **58**, pp. 363–368.
- [13] Whitham, G. B., 1974, *Linear and Nonlinear Waves*, Wiley, New York.
- [14] Liepmann, H. W., and Roshko, A., 1957, *Elements of Gas Dynamics*, Courier Dover Publications, Mineola, NY.
- [15] Tandy, J. D., Mihaly, J. M., Adams, M. A., and Rosakis, A. J., 2014, "Examining the Temporal Evolution of Hypervelocity Impact Phenomena Via High-Speed Imaging and Ultraviolet-Visible Emission Spectroscopy," *J. Appl. Phys.*, **116**(3), p. 034901.
- [16] Sugita, S., and Schultz, P. H., 2003, "Interactions Between Impact-Induced Vapor Clouds and the Ambient Atmosphere: 2. Theoretical Modeling," *J. Geophys. Res.*, **108**(E6), p. 5052.
- [17] Lee, N., Close, S., Lauben, D., Linscott, I., Goel, A., Johnson, T., Yee, J., Fletcher, A., Srama, R., Bugiel, S., Mocker, A., Colestock, P., and Green, S., 2012, "Measurements of Freely-Expanding Plasma From Hypervelocity Impacts," *Int. J. Impact Eng.*, **44**, pp. 40–49.